Reflection Symmetry Detection of Shapes Based on Shape Signatures

Thanh Phuong Nguyen, Hung Phuoc Truong, Thanh Tuan Nguyen, Yong-Guk Kim

Version of Record: https://www.sciencedirect.com/science/article/pii/S0031320322001480
Manuscript_43ba6a7af352b1b5f89d5a4cf43023f4

Reflection Symmetry Detection of Shapes Based on Shape Signatures

Thanh Phuong Nguyen[a,*], Hung Phuoc Truong[b], Thanh Tuan Nguyen[a,c], Yong-Guk Kim[b,*]

[a] *Université de Toulon, Aix Marseille Université, CNRS, LIS UMR 7020, Toulon, France*
[b] *Department of Computer Engineering, Sejong University, Seoul, Korea*
[c] *HCMC University of Technology and Education, Faculty of IT, HCM City, Viet Nam*

Abstract

We present two novel shape signature-based reflection symmetry detection methods with their theoretical underpinning and empirical evaluation. LIP-signature and R-signature share similar beneficial properties allowing to detect reflection symmetry directions in a high-performing manner. For the shape signature of a given shape, its merit profile is constructed to detect candidates of symmetry direction. A verification process is utilized to eliminate the false candidates by addressing Radon projections. The proposed methods can effectively deal with compound shapes which are challenging for traditional contour-based methods. To quantify the symmetric efficiency, a new symmetry measure is proposed over the range [0, 1]. Furthermore, we introduce two symmetry shape datasets with a new evaluation protocol and a lost measure for evaluating symmetry detectors. Experimental results using standard and new datasets suggest that the proposed methods prominently perform compared to state of the art.

Keywords: symmetry detection, reflection symmetry, LIP-signature, $\mathcal{R}$-signature, Radon

*Corresponding author
Email addresses: thanh-phuong.nguyen@univ-tln.fr (Thanh Phuong Nguyen), tphung@sejong.ac.kr (Hung Phuoc Truong), tuannt@hcmute.edu.vn (Thanh Tuan Nguyen), ykim@sejong.ac.kr (Yong-Guk Kim)

1. Introduction

Symmetry occurring both in nature and artifacts is intrinsically available around the world. Shape representation in computer vision systems can be simplified thanks to symmetrical properties. Moreover, the symmetrical structures facilitate a vision system in different tasks such as object recognition, object detection, etc. Reflection symmetry detection, also known as mirror symmetry or bilateral symmetry detection, determines if a shape can be decomposed into two parts by a line (called a symmetrical axis), i.e., this part is the reflection of the other. Afterward, symmetry detection has received increasing attention in the computer vision community [1]. Existing methods mainly deal with shape symmetry in binary images [2, 3] or symmetry of objects in natural images [4, 5]. In this paper, we will present an effective approach for understanding the symmetry of shapes by overcoming the well-known challenges of this topic: handling multiple symmetric shapes and taking into account compound shapes. It consists of two novel methods based on a solid theoretical foundation of the geometric properties in the Radon space to detect single/multiple reflection symmetries prominently. It also provides a symmetry measure to determine how good the symmetry is in every detected axis.

Compared to the prior effort [6], which has been incompletely investigated due to its limited space, this work introduces the following crucial contributions.

- A solid theoretical foundation of $\mathcal{R}$-signature about symmetric properties of a given shape is represented in Theorems 1 and 3 (see Section 4.1).
- Another efficient method is introduced by exploiting new theoretical results on LIP-signature (see Theorem 2 and Section 4.2).
- The verification process for these proposed methods is theoretically justified in Theorem 4 (see Section 4.4) to remove the false candidates.
- The proposed methods also provide a symmetry measure ranging from 0 to 1, where 1 indicates the perfect symmetry.
- Two novel public benchmark datasets are designed and named UTLN-SRA for the compound shapes with single reflection and UTLN-MRA for

those with the multiple reflections.

- A new evaluation protocol, which only needs one parameter instead of two in the previous protocol, is presented to evaluate symmetry detectors.
- A novel lost measure is also introduced for comprehensive comparisons of the competence of the reflection symmetry detectors.
- To the best of our knowledge, it is the first work based on the projection-based approach for symmetry detection. Comprehensive evaluations have validated that our proposed detectors perform well on binary images compared to state of the art.

2. Literature of reflection symmetry detection

The existing methods for reflection symmetry detection can be roughly grouped into two following main categories subject to dealing with specific input shapes. The first one contains approaches dealing with gray-scale images. Loy and Eklunhd [7] extracted and evaluated symmetrical pairs of feature points. Cicconet *et al.* [8] proposed a convolutional approach by addressing products of complex-valued Morlet-wavelet convolutions [9]. These wavelet responses were then accumulated in a voting scheme for finding reflection symmetries as a circle symmetric detection. Elawady *et al.* [10] introduced a reflection symmetry technique that relies on edge-based feature descriptors using Log-Gabor filters [11] with various scales and orientations for symmetry detection. Gnutti *et al.* [12] combined appearance and gradient information for symmetry detection in images. The second one detects reflection symmetry in binary shapes. Chaudhuri and Majumder [13] developed algorithms based on fuzzy description to detect the aides and symmetry of simply closed 2-D man-made and machine generated outlines, while Parui and Majumder [14] proposed to detect approximate locations of symmetry axes of a 2D region whose border was treated as a regular polygon in a hierarchical manner. Ogawa [15] used Hough transform [16] to detect symmetry axis in shapes by analyzing line drawings. Yip [17] then developed this approach to deal with both reflection symmetry and skew-

symmetry. Lei and Wong [18] also used Hough transform for detecting and recovering the pose of a reflection and rotational symmetry from a single weak perspective image. Nagar and Raman [19] introduced an energy minimization approach, and then an optimization on a manifold [20] is utilized for detecting approximately reflection symmetry in a set of points. Later, they exploited embedding symmetry in a graph [21] for reflection symmetry detection. Kiryati and Gofman [22] converted reflection symmetry detection into a global optimization problem, while Cornelius *et al.* [23] used local affine frames (LAFs) [24], constructed on maximally stable extremal regions, to improve the detection of symmetric objects under perspective distortion. Kazhdan [25] used Fourier transform to detect and compute reflective symmetries. Derrode and Ghorbel [26] applied Fourier-Melin transform [27, 28] to rotation and reflection symmetry estimation. Recently, Gonzalez *et al.* [2] used a 2D contour description based on Slope-Chain-Code (SCC) theory [29, 30] for symmetric/quasi-symmetric shapes.

3. Shape signatures based on Radon transform

Let $f \in \mathbb{R}^2$ be a 2D function, $\delta(.)$ be the Dirac delta-function, $L(\theta, \rho) = \{\mathbf{x} \in \mathbb{R}^2 \mid \mathbf{x} \cdot \mathbf{n}(\theta) = \rho\}$ be a straight line in $\mathbb{R}^2$ where θ is the angle made by L with the y axis, $\mathbf{n}(\theta) = (\cos\theta, \sin\theta)$, and ρ be the radial distance from the origin to L. The Radon transform [31] of f, denoted as $\mathcal{R}_f$, is a function defined on the space of lines $L(\theta, \rho)$ by calculating the line integral as follows.

$$\mathcal{R}_f(\theta, \rho) = \int f(\mathbf{x})\, \delta(\rho - \mathbf{x} \cdot \mathbf{n}(\theta))\, \mathrm{d}\mathbf{x} \tag{1}$$

In shape analysis, the function $f(.)$ is constrained to take value 1 if $\mathbf{x} \in \mathcal{D}$ and 0 otherwise, where $\mathcal{D}$ is the binary shape represented by f (see Fig. 1). Radon transform is a base for different shape descriptors [32, 33, 34, 35]. We also recall the following notions, introduced in [33], which will be used later.

Definition 1. *For projection θ, the radial distances ρ_1^θ and ρ_2^θ are respectively defined as $\rho_1^\theta = \inf\{\rho \mid \mathcal{R}_\mathcal{D}(\theta, \rho) > 0\}$ and $\rho_2^\theta = \sup\{\rho \mid \mathcal{R}_\mathcal{D}(\theta, \rho) > 0\}$. The Radon projection of $\mathcal{D}$ in the direction θ, denoted as $C_\mathcal{D}^\theta$, is defined as $\mathcal{R}_\mathcal{D}(\theta, \rho_1^\theta{:}\rho_2^\theta)$. More precisely, $C_\mathcal{D}^\theta(\rho - \rho_1^\theta) = \mathcal{R}_\mathcal{D}(\theta, \rho)$, $\forall \rho \in [\rho_1^\theta, \rho_2^\theta]$.*

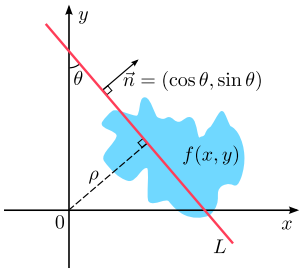

Figure 1: Radon transform

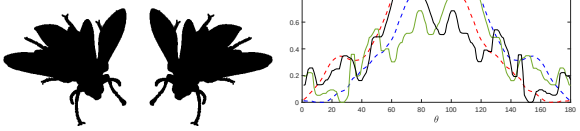

(a) Original (b) Mirrored (c) $\mathcal{R}$/LIP-signatures

Figure 2: Illustration of $\mathcal{R}$/LIP-signatures.

Hereafter, we recall two shape signatures (i.e., $\mathcal{R}$-signature and LIP-signature) based on the Radon transform.

3.1. $\mathcal{R}$-signature

Tabbone et al. [36] introduced a transform, called $\mathcal{R}$-signature (also see Fig. 2 for an illustration), for an effective shape representation as follows.

$$R_{f2}(\theta) = \int_{-\infty}^{+\infty} \mathcal{R}_f^2(\theta, \rho) d\rho \tag{2}$$

The integration, which is computed on the radial slices of the Radon image of f, makes $\mathcal{R}_{f2}$ invariant to translation and scaling, except for a multiplicative factor $\frac{1}{\alpha^3}$ resulting from the scaling factor α in f, and periodic with period π. Figure 2 shows $\mathcal{R}$ signatures calculated from a shape and its mirrored image, while Fig. 4 illustrates the robustness of $\mathcal{R}$-signatures calculated from degraded shapes. Please refer to [36] for more theoretical demonstrations and illustrated examples about the robustness of $\mathcal{R}$-signature against similarity transformations, noise, and deformations, making $\mathcal{R}$-signature useful for shape analysis.

3.2. LIP-signature

We recall in this section another shape signature, named LIP-signature (the Largest Intersection and Projection), which was introduced in [34] by addressing the geometrical properties of the studied object in the projection space (see Fig. 2 for an illustration). Let us consider a shape $\mathcal{D}$. For simplicity, we call direction θ as the direction inclined at angle θ from y axis. The following definition defines LIP-signature [34] of $\mathcal{D}$.

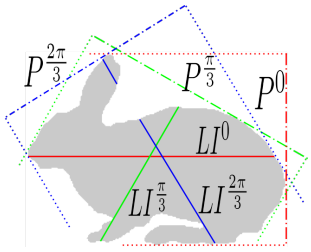

Figure 3: Calculation of LI and P in 3 directions [34].

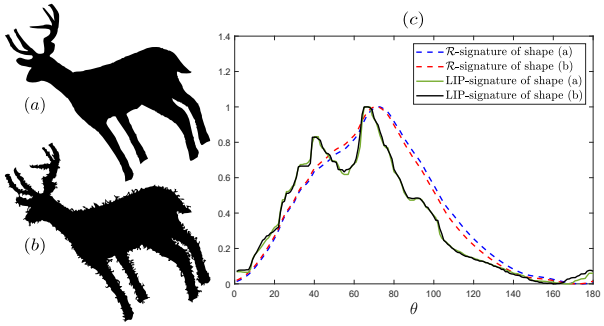

Figure 4: Robustness of shape signatures against noise and non-linear deformations.

Definition 2. *$I_s^\theta(\mathcal{D})$ is the* **intersection** *between $\mathcal{D}$ and an arbitrary line l in direction θ, and s away from the origin. $LI^\theta(\mathcal{D})$ is the* **largest intersection** *in direction θ: $LI^\theta(\mathcal{D}) = \max_s I_s^\theta(\mathcal{D})$. $P^\theta(\mathcal{D})$ is the* **projection**[1] *of $\mathcal{D}$ in direction θ on a line in direction $\theta + \frac{\pi}{2}$. Considering a set of directions $\Theta = \{\theta_i\}_{i=1}^n$, let $LIP^\theta(\mathcal{D})$ denote $\frac{LI^\theta\mathcal{D})}{P^\theta(\mathcal{D})}$. So $LIP(\mathcal{D}, \Theta) = \left\{LIP^{\theta_i}(\mathcal{D})\right\}_{i=1}^n$ is called LIP-signature of $\mathcal{D}$ over Θ.*

Figure 3 illustrates the calculation of LIP-signature by addressing its two components LI and P. Nguyen *et al.* [34] indicated that LIP-signature, containing a rich geometric interpretation of shape, is robust to additional noise and non-linear deformations. Also, LIP-signature is proved to be invariant to the translation and scaling. For a rotation of θ_0, it is shifted for a constant θ_0. Those benefits make LIP-signature be an interesting tool for shape analysis.

Figure 4 shows the robustness of LIP/$\mathcal{R}$-signatures calculated from two shapes of deer: one is a normal shape, the other is degraded from the first one by considering non-linear deformations on its contour. It could be seen that both the LIP-signatures and $\mathcal{R}$-signatures of those shapes are nearly the same. Moreover, Fig. 2 presents LIP/$\mathcal{R}$-signatures of a shape and its mirrored shape. The symmetric property of those signatures suggests us a novel approach for

[1]The terms "intersection" and "projection" indicate the cardinality of the corresponding set of pixel locations.

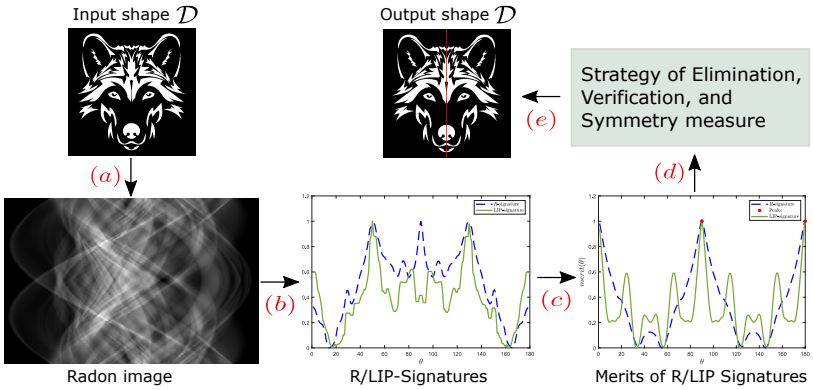

Figure 5: Main steps (in red) of our proposed shape analysis for reflection symmetry detection: (a) - Computing a Radon profile of $\mathcal{D}$, (b) - Computing R/LIP shape signatures, (c) - Computing merits of the obtained R/LIP signatures, (d) - Determining which the candidates are the best, (e) - Drawing the detected symmetry axis of $\mathcal{D}$. For a better visualization, the shape signatures are normalized to be ranged in [0,1].

symmetry detection, as presented in Section 4.

4. Proposed reflection symmetry detection

Our approach can be graphically illustrated in Fig. 5 to detect the reflection symmetry axes of an arbitrary shape. Their main idea is to convert a problem of 2D symmetry detection into a problem of 1D symmetry detection. Thereby, a given shape $\mathcal{D}$ will be addressed on the Radon space in order to obtain its Radon image, which is the base to construct its shape signatures ($\mathcal{R}$/LIP-signatures). Then the merit profile is computed from the corresponding signature in order to highlight candidates of symmetry direction. Finally, a verification process is considered to suppress the false candidates and then to return the detected symmetry directions together with symmetry measures indicating how good the symmetry is in every detected axis. Hereafter, these processes will be theoretically presented in detail.

4.1. $\mathcal{R}$-signature and reflection symmetry

We propose in this section some theoretical results about $\mathcal{R}$-signature, which can be served as a foundation for a new approach of reflection symmetry de-

tection. $\mathcal{R}$-signature is chosen as a useful tool for shape analysis because it is robust against additive noise, non-linear deformation, and it is invariant against similarity transforms [36]. The main idea is to convert the problem of detecting and measuring the reflection symmetry of an arbitrary shape $\mathcal{D}$ into measuring the reflection symmetry in its $\mathcal{R}$-signature. Due to the fact that $R_{f2}(\theta)$ is periodical of period π with respect to θ [36], it could be sufficient to only consider $\mathcal{R}$-signature on the set of projections $\Theta = [0, \pi)$. In practice, we consider a set of the discrete projections $\Theta = \{0°, 1°, \ldots, 179°\}$.

Theorem 1. *If $\mathcal{D}$ contains a reflection symmetry in direction θ_0, its $\mathcal{R}$-signature is also reflectionally symmetric at θ_0 and $\theta + \frac{\pi}{2}$.*

Proof. Let us consider Fig. 6(a), which has a reflection symmetry in direction θ_0 at axis Δ_0. Consider an arbitrary line intersection L_1 of shape $\mathcal{D}$ which lies in direction $\Delta_0 - \theta$ ($0 < \theta < \frac{\pi}{2}$) and the distance between it and the root of system coordinate is ρ (see Fig. 6(a)). It means that $L_1 = \mathcal{R}_f(\theta_0 - \theta, \rho)$. Now, let us consider L_1' as the symmetrical line segment of L_1 regarding Δ_0. Because Δ_0 is the symmetry axis of $\mathcal{D}$, L_1' must also be a line intersection of $\mathcal{D}$. We note that $L_1' = \mathcal{R}_f(\theta_0 + \theta, \rho')$ by the Radon transform definition. So, we have: $\forall \rho, \mathcal{R}_f(\theta_0 - \theta, \rho) > 0$, so: $\exists \rho' > 0, \mathcal{R}_f(\theta_0 - \theta, \rho) = \mathcal{R}_f(\theta_0 + \theta, \rho')$. It should be noted that in the above remark, if $\rho_1 \neq \rho_2$, this condition $\rho_1' \neq \rho_2'$ is also satisfied. Therefore, there exists a bijection between ρ and ρ' such that: $\mathcal{R}_f(\theta_0 - \theta, \rho) = \mathcal{R}_f(\theta_0 + \theta, \rho')$. Accordingly, $\int_{-\infty}^{+\infty} \mathcal{R}_f^2(\theta_0 - \theta, \rho) d\rho = \int_{-\infty}^{+\infty} \mathcal{R}_f^2(\theta_0 + \theta, \rho') d\rho'$. So, $\mathcal{R}_{f2}(\theta_0 - \theta) = \mathcal{R}_{f2}(\theta_0 + \theta)$, where $0 < \theta \leq \frac{\pi}{2}$. So, $\mathcal{R}_{f2}$ is reflectionally symmetric at θ_0.

Without loss of generality, suppose that $\theta < \frac{\pi}{2}$, we then denote $\theta' = \frac{\pi}{2} - \theta$. $\Delta_{\frac{\pi}{2}}$ is perpendicular with Δ_0 (see Fig. 6(a)). It should be noted that L_1 and L_1' are also reflectional regarding $\Delta_{\frac{\pi}{2}}$. These line intersections make with $\Delta_{\frac{\pi}{2}}$ an angle θ'. If we consider them in the direction $\theta_0 + \frac{\pi}{2}$ (i.e. direction of $\Delta_{\frac{\pi}{2}}$), these line intersections are calculated respectively as follows: $L_1 = \mathcal{R}_f(\theta_0 + \frac{\pi}{2} + \theta', \rho)$ and $L_1' = \mathcal{R}_f(\theta_0 + \frac{\pi}{2} - \theta', \rho')$. Because of $L_1 = L_1'$, we have $\mathcal{R}_f(\theta_0 + \frac{\pi}{2} + \theta', \rho) = \mathcal{R}_f(\theta_0 + \frac{\pi}{2} - \theta', \rho')$. Therefore, $\mathcal{R}_{f2}(\theta_0 + \frac{\pi}{2} + \theta') =$

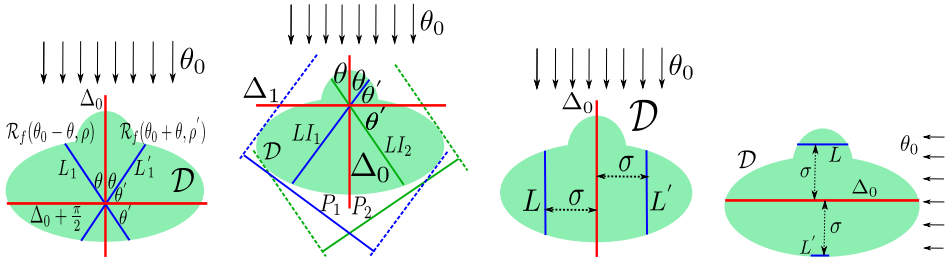

(a) Theorem 1 (b) Theorem 2 (c) Theorem 3 (d) Theorem 4

Figure 6: Illustration of our proposed theorems.

$\int_{-\infty}^{+\infty}\mathcal{R}_f^2(\theta_0+\frac{\pi}{2}+\theta',\rho)d\rho = \int_{-\infty}^{+\infty}\mathcal{R}_f^2(\theta_0+\frac{\pi}{2}-\theta',\rho)d\rho = \mathcal{R}_{f2}(\theta_0+\frac{\pi}{2}-\theta')$. Because of $\mathcal{R}_{f2}(\theta_0+\frac{\pi}{2}+\theta') = \mathcal{R}_{f2}(\theta_0+\frac{\pi}{2}-\theta')$, where $0<\theta'\leq\frac{\pi}{2}$, we have the following remark: $\mathcal{R}_{f2}$ is also reflectional symmetry at direction $\theta_0+\frac{\pi}{2}$. □

4.2. LIP-signature and reflection symmetry

We introduce in this section the similar properties, presented in Section 4.1, with LIP-signature concerning reflection symmetry detection.

Theorem 2. *If $\mathcal{D}$ contains a reflection symmetry in direction θ_0, its LIP-signature is also reflectionally symmetric at θ_0 and $\theta_0+\frac{\pi}{2}$.*

Proof. Let us consider a shape having reflection symmetry in direction θ_0 with axis Δ_0. Let LI_1 and LI_2 (resp. P_1 and P_2) denote respectively the longest intersection (resp. the projection) of $\mathcal{D}$ in direction $\theta_0-\theta$ and $\theta_0+\theta$ (also see Fig. 6(b)). Thanks to the symmetric property of $\mathcal{D}$, we obtain $LI_1 = LI_2$, and $P_1 = P_2$. It implies that $LIP^{\theta_0-\theta}(\mathcal{D}) = LIP^{\theta_0+\theta}(\mathcal{D})$, $\forall\theta\in[0,\frac{\pi}{2})$. Consequently, LIP-signature is reflectionally symmetric at θ_0.

Let us denote $\theta' = \frac{\pi}{2}-\theta$. It should be noted that we have those properties $LI^{\theta}(\mathcal{D}) = LI^{\pi+\theta}(\mathcal{D})$ and $P^{\theta}(\mathcal{D}) = P^{\pi+\theta}(\mathcal{D})$ thanks to their definitions (see Definition 2). Therefore, LI_1 and P_1, which are the longest intersection and projection of $\mathcal{D}$ in direction $\theta_0+\pi-\theta$ respectively, are also the corresponding parameters in direction $\theta_0+\frac{\pi}{2}+\theta'$. On the other hand, we can rewrite that LI_2 and P_2 are respectively the longest intersection and projection of $\mathcal{D}$ in

direction $\theta_0+\theta = \theta_0+\frac{\pi}{2}-\theta'$. It means that $LIP^{\theta_0+\frac{\pi}{2}+\theta'}(\mathcal{D}) = LIP^{\theta_0+\frac{\pi}{2}-\theta'}(\mathcal{D})$, $\forall\theta' \in [0, \frac{\pi}{2})$. So, LIP-signature is also reflectionally symmetric at $\theta_0 + \frac{\pi}{2}$. □

4.3. Merit profile of $\mathcal{R}$-signature and LIP-signature

It could be deduced from Theorems 1, 2 that $\mathcal{R}$-signature and LIP-signature have similar properties concerning reflection symmetry. Thanks to those, we can detect candidates of symmetry direction of a shape by verifying reflectional symmetrical properties of these signatures. The problem of reflection detection, which is now converted from 2D domain to 1D domain, is evidently less complicated to resolve. We propose then to measure the degree of reflection symmetry at each position of a 1D signal by comparing the similarity between it and its circular inverse signal at this position by considering the following definition.

Definition 3. *Given $x = \{x_1, x_2, \ldots, x_n\}$, a vector of n elements. $F^i(x)$ (resp. $B^i(x)$), which is called forward (resp. backward) circular shift of x of step i, is defined as follows: $F^i(x) = \{x_i, x_{i+1}, \ldots, x_n, x_1, \ldots, x_{i-1}\}$ (resp. $B^i(x) = \{x_i, x_{i-1}, \ldots, x_1, x_n, \ldots, x_{i+1}\}$). Specially, the inversion of x, called $I(x)$, is defined by $I(x) = B^n(x)$*

It is evident that vector x has a reflection symmetry at index k if and only if $F^k(x)$ and $B^k(x)$ are identical. In order to measure the degree of reflection symmetry of x at position k, we propose to estimate the similarity between $F^k(x)$ and $B^k(x)$. There exist several similarity distances for this purpose in the literature. Empirically, in order to obtain a robust measurement, we propose to use Pearson's correlation [37] to measure those similarities. For simplicity, let us consider two vectors X and Y having the same dimensionality. The similarity between them is defined as follows.

$$\Omega(X,Y) = \frac{\sum_{j=1}^{n}(X-\overline{X})(Y-\overline{Y})}{\left(\sum_{i=1}^{n}(X-\overline{X})^2 \sum_{i=1}^{n}(Y-\overline{Y})^2\right)^{1/2}} \tag{3}$$

where n is the number of elements in vector X; $\overline{X}$ and $\overline{Y}$ are respectively the mean values of X and Y. The values of $\Omega(X,Y)$ range from -1 to $+1$ estimating how X is similar to Y.

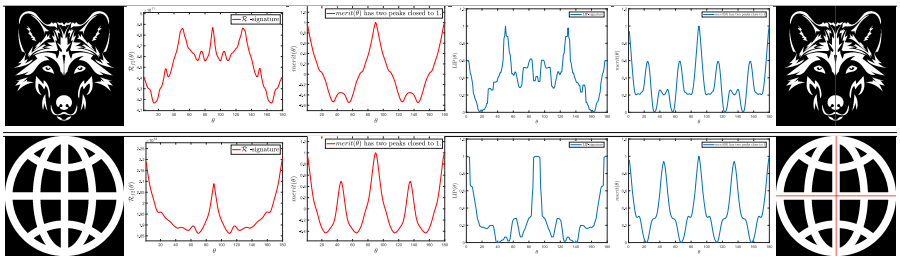

Figure 7: Merit profiles are constructed from the $\mathcal{R}$-signature and LIP-Signature of shapes. Their peaks, which are close to 1, correspond to candidates of reflection symmetry direction. From the left column to the right column: Input shape, $\mathcal{R}$-signature, Merit profile of $\mathcal{R}$-signature, LIP-signature, Merit profile of LIP-signature, Reflection axis. The 1^{st} row illustrates single reflection symmetry, while the 2^{nd} one is for multiple reflection symmetry.

Therefore, the analysis in Section 4.1 suggests an effective algorithm for reflection symmetry detection of a shape by considering the merit profile calculated from its signatures (i.e., $\mathcal{R}$-signature, LIP-signature). The main idea is to measure the similarity between its forward and backward circular shifts of each angle θ_0. If this similarity is perfect, angle θ_0 is a candidate for a reflectionally symmetric direction. Fig. 7 presents an illustration of merit profiles of two shapes constructed from their signatures. The first row presents a shape having only one axis of reflection symmetry, while the second one illustrates a shape having two reflection axes that are orthogonal. It could be noted that the merit profiles of these shapes also have two peaks close to 1. In addition, it could be pointed out the following findings in accordance with Theorems 1, 2.

- If the axis of reflection symmetry is in direction θ_0, its merit profile has two corresponding peaks close to 1 at θ_0 and $\theta_0 + \frac{\pi}{2}$, respectively.
- A peak close to 1 at direction θ_0 does not mean that the given shape has a reflection symmetry in that direction. It leads to our proposed strategy for eliminating the false directions in Section 4.4.
- The merit profile, which is smooth, guarantees that it has exactly two close-to-1 peaks for each symmetry direction. Therefore, the problem of multiple detections is avoided in our approach.

4.4. Elimination of false directions of reflection symmetry

In order to detect the actual symmetry directions of shape $\mathcal{D}$ by considering its merit profile, we must remove the false candidates predicted by Theorems 1 and 2. The following verification process is proposed for this purpose. Our solution, based on the following Theorems 3 and 4, is to check if the Radon projection in the candidate direction ($C_{\mathcal{D}}^{\theta_0}$) is symmetrical.

Theorem 3. *If $\mathcal{D}$ contains reflection symmetry in direction θ_0, there exists ρ_0 such that $\mathcal{R}_f(\theta_0, \rho)$ is reflectionally symmetric at ρ_0 where ρ is variable.*

Proof. Let us consider Fig. 6(c), which presents a shape $\mathcal{D}$ and its axis of reflection symmetry Δ_0 in direction θ_0. Without loss of generality, let us suppose that $\mathcal{D}$ is in the first quadrant of the coordinate system. The distance between Δ_0 and the root of the coordinate system is ρ_0. Consider now an arbitrary line intersection with $\mathcal{D}$ (i.e., L) in direction θ_0 at the left side of Δ_0. The distance between L and Δ_0 is σ. L' is the symmetrical segment of L regarding Δ_0 (see Fig. 6(c) for the illustration of all those notations). Because $\mathcal{D}$ has Δ_0 as its axis of reflection symmetry, L' must also be a line intersection line $\mathcal{D}$ in direction θ_0. It is evident that the distance between L (resp. L') and the root of the coordinate system is $\rho - \sigma$ (resp. $\rho + \sigma$) respectively. In addition, L and L' are the line intersections of $\mathcal{D}$ in direction θ_0. It could be deduced the following remarks: $L = \mathcal{R}_f(\theta_0, \rho - \sigma)$ and $L' = \mathcal{R}_f(\theta_0, \rho + \sigma)$. Moreover, thanks to $L = L'$, we obtain this result $\mathcal{R}_f(\theta_0, \rho - \sigma) = \mathcal{R}_f(\theta_0, \rho + \sigma)$, where $0 < \sigma < \rho$. It means that $\mathcal{R}_f(\theta_0, \rho)$ is reflectionally symmetric at ρ_0. □

Theorem 4. *If $\mathcal{R}_f(\theta_0, \rho)$ is not reflectional symmetry regarding ρ, $\mathcal{D}$ is not reflectional symmetry in direction θ_0*

Proof. Let us suppose that $\mathcal{D}$ is reflectional symmetry in direction θ_0 with its axis of reflection symmetry Δ_0 (see also Fig. 6(d)). We denote that ρ_0 is the distance between Δ_0 and the root of the coordinate system. Because $\mathcal{R}_f(\theta_0, \rho)$ is not reflectional symmetry regarding ρ, there exists then σ such that $\mathcal{R}_f(\theta_0, \rho_0 - \sigma) \neq \mathcal{R}_f(\theta_0, \rho_0 + \sigma)$. Considering the intersection lines of $\mathcal{D}$ in direction θ_0 at

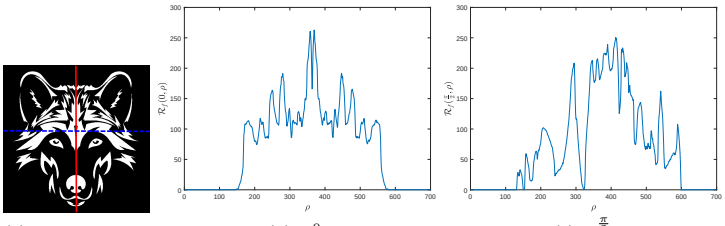

(a) Input shape $\mathcal{D}$ (b) $C^0_{\mathcal{D}}$ (c) $C^{\frac{\pi}{2}}_{\mathcal{D}}$

Figure 8: Verification of reflection symmetry based on Radon projection.

two sides of Δ_0 (i.e., L and L') such that the distances between them and Δ_0 are σ. It should be noted that $L = \mathcal{R}_f(\theta_0, \rho_0 + \sigma)$ and $L' = \mathcal{R}_f(\theta_0, \rho_0 - \sigma)$. Therefore, $L \neq L'$. It means that L and L' cannot be symmetrical regarding Δ_0. Accordingly, $\mathcal{D}$ cannot accept Δ_0 as its symmetrical axis. This contradiction proves the conclusion of the proposed theorem. □

Theorems 3 and 4 allow us to introduce a criterion, based on Radon projection $C_{\mathcal{D}}(\theta_0)$ (i.e. $\mathcal{R}_f(\theta_0, \rho)$), for checking if a direction candidate θ_0 is reflection symmetry. Based on this solution, θ_0 is a good symmetry direction if and only if $C_{\mathcal{D}}(\theta_0)$ is reflectionally symmetric. Fig. 8 illustrates how to verify reflection symmetry at direction candidates 0 and $\frac{\pi}{2}$, which have been detected by addressing their merit profiles. At direction 0 (illustrated by the red line of Fig. 8(a)[2], the Radon projection ($C^0_{\mathcal{D}}$ or $\mathcal{R}_f(0, \rho)$) is reflectionally symmetric. However, at the direction $\frac{\pi}{2}$ (the blue dotted line of Fig. 8(a), the corresponding Radon projection $C^{\frac{\pi}{2}}_{\mathcal{D}}$ is not reflectionally symmetric.

4.5. Verification process and symmetry measure

In order to measure symmetrical properties of Radon projections presented in Section 4.4, we also use Pearson's correlation coefficient, presented in Eq. 3, to determine how symmetrical confidence the considered shape is in direction θ. For the verification of candidates, Radon projection $C^{\theta}_{\mathcal{D}}$ is symmetrical if and only if it and its inverse version $I(C^{\theta}_{\mathcal{D}})$ is identical. Therefore, we can estimate

[2]In the Radon space, the vertical line is in direction 0°.

the similarity between $C_{\mathcal{D}}^{\theta}$ and $I(C_{\mathcal{D}}^{\theta})$ to define the symmetry measure of $\mathcal{D}$ at direction θ as follows.

$$\Psi_{\mathcal{D}}(\theta) = \Omega(C_{\mathcal{D}}^{\theta}, I(C_{\mathcal{D}}^{\theta})) \tag{4}$$

The value of Eq. 4, indicating the symmetric degree of $C_{\mathcal{D}}^{\theta}$, is between -1 and $+1$. Because the negative range means that there is no symmetry at all, the obtained measure $\Psi_{\mathcal{D}}(\theta)$ should be located from 0 to 1 for an effective symmetry measure in practice. Thereby, a threshold $\tau \in (0, 1)$ would be used to suppress the non-significant candidates of symmetry (see Alg. 2).

4.6. Proposed methods for symmetry detection in binary images

We propose then in this section two methods[3] for reflection symmetry detection based on the theoretical foundation, as presented in the previous sections. Indeed, the main problem of reflection symmetry detection is to determine the directions of reflection. If a direction θ_0 is detected, the axis of reflection can be easily defined by a line in this direction passing through the centroid of the studied shape. Alg. 1 presents a moment-based method for detecting the centroid of an arbitrary binary shape.

Algorithm 1 Detection the centroid of a shape $\mathcal{D}$.

Input: $\mathcal{D}$ – arbitrary shape, **Output:** c – detected centroid

1: $sX = \sum_{p \in \mathcal{D}} p_x$; $sY = \sum_{p \in \mathcal{D}} p_y$; $s = \sum_{p \in \mathcal{D}} 1$

2: $c = (\frac{sX}{s}, \frac{sY}{s})$

We then concentrate on the detection of directions of reflection symmetry. The theoretical foundation in Sections 4.1, 4.3, and 4.4 allows us to introduce two different methods in Alg. 2 for solving this problem. They share together the similar properties as presented in Sections 4.1 and 4.2. As intuitively illustrated in Fig. 5, the shape signatures of a given shape $\mathcal{D}$ are firstly calculated (i.e., $\mathcal{R}$-signature and LIP-signature). Second, their corresponding merit profiles are constructed for detecting direction candidates which are located as the

[3] A simple MATLAB code of our proposed detectors using $\mathcal{R}$/LIP-signatures is available at: `http://tpnguyen.univ-tln.fr/download/UTLN-Reflection/R_LIP_MATCode`.

close-to-1 peaks of the merit profiles. Then, a verification process is addressed to eliminate the false direction candidates. If the obtained measure is higher than a threshold, the direction candidate is then indicated as a direction of a reflection axis together with its symmetry measure. Indeed, the proposed methods need two parameters corresponding to two thresholds for eliminating the non-significant candidates. The first one τ_1 is used to remove the non-significant peaks detected from the merit profile, while the second one τ_2 is the symmetry measure which is used to suppress the false candidates of symmetry directions in the next step. Theoretically, in order to detect the actual reflection symmetry, we have the following condition: $\tau_1 = \tau_2 = 1$. In practice, these parameters can be replaced by a unique threshold τ for the simplification as addressed in Alg. 2. It is recommended to consider $\tau \geq 0.65$ to guarantee the quality of the symmetry detection.

5. Quantitative experiments and evaluations

5.1. Datasets

5.1.1. MPEG-7 dataset

MPEG-7 [38] was generally composed for shape analysis techniques: shape matching, classification, etc. The dataset consists of 70 classes, 20 binary shapes for each class. In 2019, Gonzalez *et al.* [2] attempted to address several shapes of MPEG-7 for reflection symmetry detection. Accordingly, the selected set includes both symmetrical and quasi-symmetrical shapes which their ground-truth (GT) symmetrical axes were indicated by a group of concerned researchers. Fig. 9(a) illustrates several symmetrical shapes, while Fig. 9(b) is for some of the quasi-symmetrical shapes, where their GT axes are drawn in red lines.

5.1.2. Our UTLN Reflection datasets

It should be noted that the shapes of MPEG-7 [38] are not ideal for evaluating detectors of reflection symmetry. Indeed, they are not actually symmetrical shapes in many cases. Therefore, the corresponding ground truth, which is

Algorithm 2 Reflection symmetry detection of a shape $\mathcal{D}$.

Input: $\mathcal{D}$ – arbitrary shape, τ – threshold for symmetry detection, *method* – TRUE: LIP-signature, FALSE: $\mathcal{R}$-signature

Output: n – a number of detected symmetric axis, Υ – reflection symmetry measures Δ – a set of detected symmetric directions

$\Theta = \{0°, 1°, \ldots 179°\}$; $merit = []$; $\psi = n = 0$ //Initially, no symmetry found
if *method* **then**
  Construct $\Phi(\mathcal{D}, \Theta)$ as LIP$(\mathcal{D}, \Theta)$; //LIP-signature of $\mathcal{D}$ over Θ
else
  Construct $\Phi(\mathcal{D}, \Theta)$ as $R_{f2}(\mathcal{D}, \Theta)$; //$\mathcal{R}$-signature of $\mathcal{D}$ over Θ
end if
for $\theta = 0° \ldots 179°$ **do**
  $merit(\theta) = \Omega\big(F^{\theta}_{\zeta}(\Phi(\mathcal{D}, \Theta)), B^{\theta}_{\zeta}(\Phi(\mathcal{D}, \Theta))\big)$;
end for
Detect *peaks* and *ids*; //the peaks of *merit* that are greater than τ (values and indices respectively)
for $k = 1 \ldots length(peaks)$ **do**
  $\theta = ids(k)$;
  Calculate $\Psi_{\mathcal{D}}(\theta)$ using Eq. (4).
  if $\Psi_{\mathcal{D}}(\theta) > \tau$ **then**
    $n = n + 1$; //found a new axis of reflection symmetry
    $\Delta(n) = ids(k)$;
    $\Upsilon(n) = \Psi_{\mathcal{D}}(ids(k))$; //corresponding symmetry measure
  end if
end for

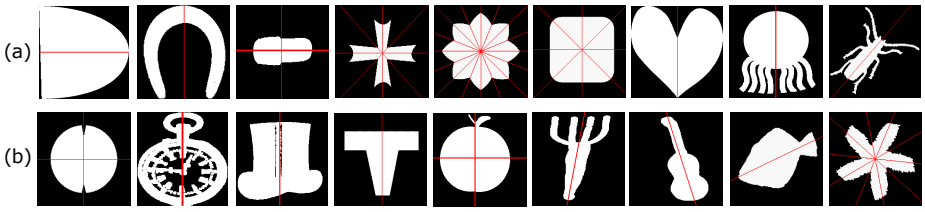

Figure 9: Several selected shapes of MPEG-7 for evaluations of reflection symmetry detection: (a) symmetrical and (b) quasi-symmetrical shapes.

manually defined by human vision, may not be unique and disputable in several cases. This remark can be evidently observed in Fig. 9(b). Furthermore, because those of MPEG-7 are single contour shapes, they are not challenging definitely. It is necessary to consider *how well a symmetry detector works on*

Table 1: A summary of our proposed datasets

	UTLN-SRA	**UTLN-MRA**
# Shape Images	210	100
# Mirror Symmetry Axes	210	535

complex/compound shapes which the traditional contour-based methods [2] either have not been validated on or could not perform well. On the other hand, there is only one symmetrical axis for every shape of MPEG-7. Therefore, this fails to evaluate *how a symmetry detector works on a multiple symmetric shape* and *how good the detection is when the number of symmetrical axes is unknown.*

Addressing those above shortcomings, we introduce in this paper a new dataset for evaluation of reflectional symmetry detection, called "UTLN Reflection dataset"[4], which is created by collecting free images on the Internet. Our dataset contains two test suites: UTLN-SRA (Single Reflection Axis) and UTLN-MRA (Multiple Reflection Axes). The first one, which contains shapes having a single reflection symmetry (see Fig. 10(a)), is designed to evaluate the detection of the best reflection axis. The second one, which addresses shapes of multiple reflection axes (see Fig. 10(b), is served for evaluating the detection of multiple reflection axes. Moreover, UTLN-SRA and UTLN-MRA contain both simple and compound shapes. We asked five experts in the Computer Vision field to annotate the datasets. The final ground-truth (GT) axes should be agreed by all experts. Table 1 shows the total number of symmetry axes for each dataset.

5.2. Evaluation protocols

5.2.1. Existing evaluation protocol

Evaluation of current methods is based on the following protocol [7, 4, 10]. It should be noted that this must be customized to deal with shapes containing multiple axes of reflection symmetry. With each detection result, the angle Δ_θ between the detected symmetry axis and the ground-truth axes θ_G is measured.

[4]It is available at: `http://tpnguyen.univ-tln.fr/download/UTLN-Reflection`.

Figure 10: Several samples of UTLN-SRA (a) and UTLN-MRA (b) where their GT axes are drawn in red lines.

Moreover, the Euclidean distance Δ_d from the detected center c_D to the ground-truth line segment θ_G is also determined. A reflection symmetry candidate is considered as a correct axis corresponding to the segment θ_G (a true positive, or TP) if satisfying the following conditions:

$$\Delta_\theta = |\theta_D - \theta_G| \leq \gamma \text{ and } \Delta_d = d(c_D, \theta_G) \leq \mu \tag{5}$$

Accordingly, the Precision and Recall rates are defined by the numbers of TP, false positive (FP), and false negative (FN). F1-score is then defined from them as the overall accuracy.

$$\text{Precision} = \text{TP} \;/\; (\text{TP} + \text{FP}); \text{Recall} = \text{TP} \;/\; (\text{TP} + \text{FN}) \tag{6}$$

$$\text{F1-score} = 2(\text{Precision} \times \text{Recall}) \;/\; (\text{Precision} + \text{Recall}) \tag{7}$$

Therein, FP is for the mirror symmetry candidates not to be close to any of ground-truth segments, while FN is for none of the right symmetry candidates. However, the pair (γ, μ) in the evaluations was investigated in various values, depending on the ability of each method (see Table 2 for several constraint thresholds). Besides, the constant thresholds in [7] are not flexible since the threshold of μ should adapt to the size of a given image.

Table 2: A pair of constraint thresholds reported in several methods, where l_{det} and l_{GT} are the lengths of the detected axis and the GT respectively; (W, H) is the size of a given image.

Method	γ	μ
Loy *et al.* [7]	5	5
Cicconet *et al.* [4]	3	$0.025min\{W, H\}$
Gonzalez *et al.* [2]	10	10
Cicconet *et al.* [8]	10	$0.2min\{l_{det}, l_{GT}\}$
Elawady *et al.* [10]	3	$0.025min\{W, H\}$
Cicconet *et al.* [39]	3	$0.2min\{l_{det}, l_{GT}\}$

In order to complete this protocol, we propose to consider hereunder the total loss of each metric (e.g., Δ_θ and Δ_d) as complementary criteria for evaluating methods. It should be noted that our proposed metrics are designed for shapes having multiple reflection axes. Let us consider the loss of symmetry detection in the k^{th} shape image of a dataset. We suppose that $\{\theta_D^{j,k}\}_{j=1}^{L_k}$ is a set of L_k directions of symmetrical axes resulted from the k^{th} shape, while $\{\theta_G^{i,k}\}_{i=1}^{M_k}$ is a set of M_k directions of the ground-truth axes. Each detected axis is assigned to the closest ground-truth axis in terms of direction difference. We then calculate the loss for each ground-truth axis. If none of the detected axes is assigned to any ground-truth axes, the loss is maximal (i.e., equal to 1). In other words, the loss is the total of angle differences between the ground-truth axis and its corresponding detected axes which are normalized by the number of the ground-truth axes. Eq. 11, based on Eqs. (8) and (9), defines the angle loss for the i^{th} ground-truth axis of the k^{th} shape (GT_k^i). Since the shape contains M_k ground-truth axes, the maximal angle difference is then calculated by $\frac{180}{2M_k} = \frac{90}{M_k}$. Therefore, the angle difference between the ground-truth axis and every its detected axis is then weighted by $\frac{M_k}{90}$. Similarly, Eq. (12), which is based on Eqs. (8) and (10), defines the distance loss $d^{j,k}$ for the distance from the j^{th} detected axis of the k^{th} shape to the center/position of the ground-truth axis. It is then weighted by $\frac{2}{\sqrt{W^2+H^2}}$ since the maximal distance loss is $\frac{\sqrt{W^2+H^2}}{2}$.

$$GT_k^i = \{j\}_{1\leq j\leq L_k}, \text{where } i = \arg\min_m |\theta_D^{j,k} - \theta_G^{m,k}| \tag{8}$$

$$\delta_\theta^{j,k} = |\theta_D^{j,k} - \theta_G^{i,k}|\frac{M_k}{90} \tag{9}$$

$$\sigma_d^{j,k} = d^{j,k}\frac{2}{\sqrt{W^2+H^2}} \tag{10}$$

The losses of angle and distance for each ground-truth axis are defined as

$$\Delta_\theta^{i,k} = \begin{cases} \sum\limits_{j\in GT_k^i} \delta_\theta^{j,k}, \text{ if } |GT_k^i| > 0 \\ 1, \text{otherwise} \end{cases} \tag{11}$$

$$\Delta_d^{i,k} = \begin{cases} \sum\limits_{j\in GT_k^i} \sigma_d^{j,k}, \text{ if } |GT_k^i| > 0 \\ 1, \text{otherwise} \end{cases} \tag{12}$$

So, we propose to define hereunder the total losses on a dataset with N shapes.

$$loss_{\Delta_\theta} = \frac{1}{N}\sum_{k=1}^{N}\frac{1}{M_k}\sum_{i=1}^{M_k}\Delta_\theta^{i,k} \tag{13}$$

$$loss_{\Delta_d} = \frac{1}{N}\sum_{k=1}^{N}\frac{1}{M_k}\sum_{i=1}^{M_k}\Delta_d^{i,k} \tag{14}$$

As can be seen from Table 2, the pair of constraint thresholds (γ, μ) in the existing methods [4, 2, 7, 8, 10, 39] was addressed in various values for

computing measures. So it cannot make sense to an overall assessment of the detection competence. Inspired by the constraint thresholds of the former works [4, 10], the pair of thresholds (γ, μ) in the evaluation stage of this work will be addressed as $(\gamma, \mu) = (3, 0.02\sqrt{W^2 + H^2})$ for an objective judgment.

5.2.2. Proposed evaluation metric

The previous evaluation protocol considers two metrics (the angle Δ_θ and the distance Δ_d) for a binary decision of detecting reflection symmetry. Thus, several methods reported their own thresholds for evaluation, as shown in Table 2. Addressing independently those two metrics leads to the following shortcomings. First, this requires two different thresholds, which are too excessive for a binary decision. Second, they are not independent since a good symmetry detection has to require the small values of both metrics. It would be better if there is a unified metric of these relations. We introduce hereunder a new metric for the evaluation of symmetry detection.

Let *U-loss* be the overall *unified loss* of a method by examining both losses of angle ($\Delta_\theta^{i,k}$) and distance ($\Delta_d^{i,k}$) for the ground-truth axes as follows:

$$U\text{-}loss = \frac{1}{N}\sum_{k=1}^{N}\frac{1}{M_k}\sum_{i=1}^{M_k}\sqrt{(\Delta_d^{i,k})^2 + (\Delta_\theta^{i,k})^2} \tag{15}$$

Our *U-loss* is inspired by the distance of two data points in a 2D Euclidean space (angle and center of an axis). In this space, a data point is represented by two components, including angle and center/position of the axis. Each loss component (Δ_θ and Δ_d) is to compute the correlation between the detected axes and the ground-truth ones. Therefore, our *U-loss* could adequately represent the correlation of the angle and distance losses.

In other aspects, F1-score is based on the binary decision in consideration of TP, FP, and FN, while *U-loss* is the accumulation of loss metrics for every ground-truth axis. In other words, if a method detects many FN axes or FP axes with large dissimilarity (the angle loss $\Delta_\theta^{i,k}$ and the distance loss $\Delta_d^{i,k}$), it will lead to a larger total loss. In this case, *U-loss* will increase faster than F1-score due to Eqs. 11 and 12. So, *U-loss* is more appropriate to evaluate methods in terms of the accurateness of detected axes.

Table 3: Evaluation with the relevant metrics.

	Dataset	MPEG-7		UTLN-SRA		UTLN-MRA	
	τ	**F1-score**	***U-loss***	**F1-score**	***U-loss***	**F1-score**	***U-loss***
$\mathcal{R}$-detector	0.65	0.76923	0.34226	0.99524	**0.00099**	0.84799	0.27109
	0.70	0.81013	0.33828	0.99524	**0.00099**	0.87089	0.23862
	0.75	**0.86713**	**0.33550**	0.99524	**0.00099**	0.89121	0.18395
	0.80	0.86331	0.35500	0.99524	**0.00099**	0.89865	0.16024
	0.85	0.85926	0.40796	**0.99761**	0.00752	0.89918	**0.15279**
	0.90	0.82258	0.55325	0.99522	0.01425	**0.90178**	0.15623
	0.95	0.72727	0.70235	0.97059	0.08160	0.89307	0.18215
LIP-detector	0.65	**0.78205**	**0.24470**	**0.99284**	**0.00772**	0.91622	0.19156
	0.70	0.77922	0.24621	**0.99284**	**0.00772**	0.92559	0.16969
	0.75	0.77632	0.26806	**0.99284**	**0.00772**	0.92896	0.15664
	0.80	0.75862	0.28494	**0.99284**	**0.00772**	**0.93135**	**0.14613**
	0.85	0.75524	0.35296	0.99281	0.02092	0.92279	0.15053
	0.90	0.78195	0.49977	0.98795	0.03425	0.92218	0.16104
	0.95	0.69421	0.67045	0.94472	0.14868	0.86407	0.24047

5.3. Assessments of shape signatures

5.3.1. Efficient strategies of elimination and verification

As mentioned in Sections 4.4 and 4.5, we located the threshold $\tau \geq 0.65$ for the refining strategies to point out the right reflection symmetries from the detected candidates. Hereafter, we investigate its influence on the processes of elimination and verification. Accordingly, we address different values $\tau \in \{0.65, 0.7, 0.75, 0.8, 0.85, 0.9, 0.95\}$ for reflection symmetry detection on binary shapes of datasets: MPEG-7 [38], UTLN-SRA, and UTLN-MRA. Table 3 shows the detection performances using $\mathcal{R}$-signature and LIP-signature. It can be observed that the reflection symmetry detection with the $\mathcal{R}$-signature generally outperforms that with the LIP-signature on the simple shapes of MPEG-7 and the compound shapes with a single reflection axis (i.e., UTLN-SRA), but not on the compound multiple-reflection-axis ones in UTLN-MRA. The detection results on the various levels of τ allow us to make a suggestion for overall adaptation. It means that the unique threshold $\tau = 0.8$ would be recommended for the remaining evaluations of both our proposed analyses of the shape signatures. For convenience in further presentation, we would like to name our shape-signature-based detectors as follows: $\mathcal{R}$-detector for the shape analysis based on $\mathcal{R}$-signature while LIP-detector for the technique using LIP-signature.

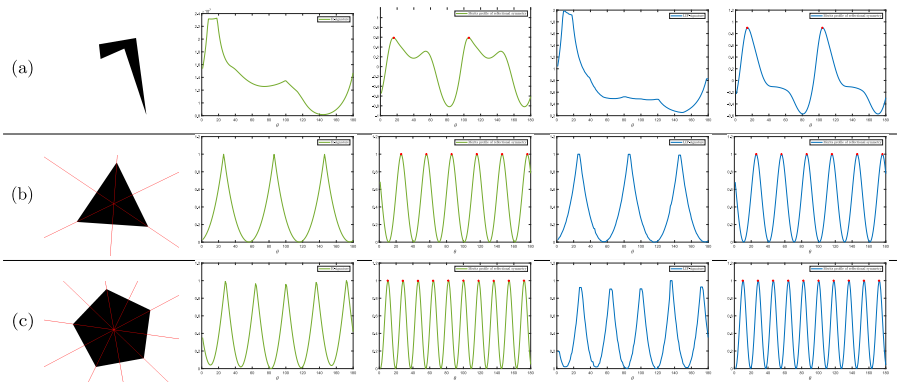

Figure 11: Synthetic analysis of a arbitrary shape (a) and regular polygons (b, c). From the left column to the right column: Shape and its detected axes, $\mathcal{R}$-signature, Merit profile of $\mathcal{R}$-signature, LIP-signature, Merit profile of LIP-signature.

5.3.2. Robustness to deformation and noise

We will evaluate $\mathcal{R}$-signature and LIP-signature on synthetic shapes to verify their behaviors of robustness in non-linear deformations. To this end, we address different polygons in variants of size and orientation. Fig. 11 shows the obtained results with different synthetic shapes, i.e., arbitrary (a) and regular polygons (b, c). Absolutely, no reflection symmetry would be pointed out regarding the detecting analysis for the non-symmetric shape (a) in Fig. 11. This is because the merit profile of its $\mathcal{R}$-signature gives the highest value at only 0.59, while that of its LIP-signature has two close-to-1 peaks, but these false symmetry candidates could have been eliminated by our verification strategies as presented in Sections 4.4 and 4.5. Besides, it should be noted that for the 3-polygon (b) and 5-polygon (c) shapes, the number of symmetry candidates based on their corresponding merit profiles is twice the number of the actual axes. Half of them could have been removed after utilizing our proposed strategies of the simple verification to eliminate the false ones.

Regarding the prominent ability of noise resistance of our proposed shape signatures, let us consider two representative compound shapes, e.g., a single-axis shape of UTLN-SRA (see Fig. 12(a)) and a multi-axis one of UTLN-MRA (see Fig. 12(b)), in three heaviest levels of signal-to-noise ratio (SNR),

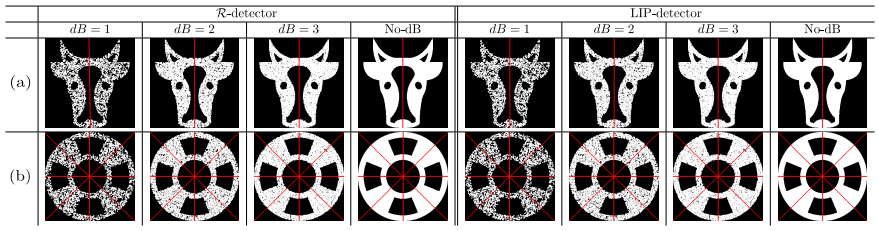

Figure 12: Robustness of our proposed detectors in different SNR levels.

Table 4: Evaluation of noise-resistant competence on UNTL-SRA.

	$dB = 1$		$dB = 2$		$dB = 3$		No-dB	
Method	**F1-score**	***U-loss***	**F1-score**	***U-loss***	**F1-score**	***U-loss***	**F1-score**	***U-loss***
Loy *et al.* [7]	0.814286	0.089609	0.919048	0.057995	0.952381	0.045771	0.968825	0.059159
Cicconet *et al.* [4]	**0.961905**	**0.023734**	0.961905	0.024617	0.966667	0.018714	0.995238	0.008015
Cicconet *et al.* [8]	0.885714	0.057435	0.923810	0.037521	0.928571	0.037003	0.928571	0.036914
Elawady *et al.* [10]	0.315036	0.385963	0.695238	0.191006	0.842857	0.122939	0.971429	0.032242
Cicconet *et al.* [39]	0.797136	0.151005	0.851675	0.119836	0.846154	0.125940	0.867470	0.106295
Our $\mathcal{R}$-detector	0.924620	0.168220	**0.978520**	**0.022734**	**0.990430**	**0.018450**	**0.995240**	**0.000998**
Our LIP-detector	0.873680	0.288310	0.963680	0.062342	0.990430	0.017967	0.992840	0.007718

i.e., $\text{SNR}_{dB} = \{1, 2, 3\}$. We then address our shape-signature-based detectors to determine reflection symmetry candidates of these SNR-noised shapes. It can be seen from Fig. 12 that our detectors have been definitely resistant to the heavy noise levels on these compound shapes. Furthermore, we also investigate the noise-resistant ability on the single-axis shapes of UTLN-SRA. Table 4 verifies that our proposed detectors have better competence in noise resistance compared to other methods, except the detector of Cicconet *et al.* [4] in more stability with F1-score decrease by 0.03. Indeed, the performance of the $\mathcal{R}$-detector and LIP-detector has just decreased by about 0.07 and 0.12 F1-score respectively, while the other detectors have a sharp reduction.

5.4. Inadequacy of contour-based techniques

As reported by Gonzalez *et al.* [2], their contour-based approach obtained the significant detection results on the simple contour shapes of MPEG-7 [38]. Nevertheless, on the compound shapes, the competence of the contour-based detector can be generally limited because of their inherent analysis techniques in the company of two main challenging properties of the compound shapes: multi-complex contours and multiple reflection symmetry.

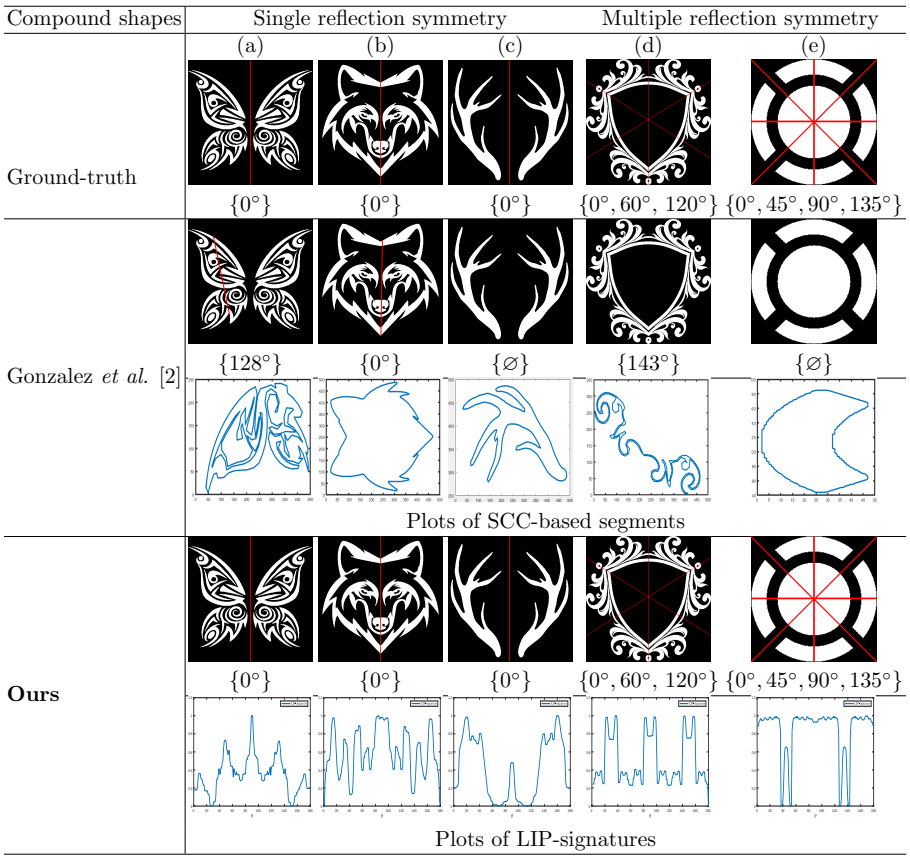

Figure 13: Our detection on compound shapes compared to a contour-based analysis [2].

Indeed, let us consider some compound shapes as shown in Fig. 13, where shapes (a,b,c) are for the single-reflection symmetry while (d,e) are for the multiple-reflection. We address the parameters of Gonzalez *et al.* [2] as follows: $\kappa = 0.614$ and $\rho = 0.042$ inferred subject to the input of the compound shapes while being the default for the rest. It can be seen in Fig. 13 that our algorithm can detect better than that of Gonzalez *et al.* [2]. The contour-based analysis could not do exactly due to the fact that just one part of the shape's contour was located and segmented by the Slope-Chain-Code (SCC) theory [29, 30]. Indeed, the compound shapes (a,b,c,e) are established by many disjointed contours. These shapes are inflectional symmetry if all of the disjointed contours have to

be analyzed together. Here, there was an accidentally correct detection for shape (b) because of its inner decorative contour with natural reflection symmetry. Due to the inadequacy of the contour-based approach [2], we would like to omit its evaluation on the compound shapes in UTLN-SRA and UTLN-MRA datasets. Consequently, it could be asserted that our proposal is more adaptive than the recent contour-based analysis [2]. This has definitely consolidated the interest of our proposal.

5.5. Comprehensive comparison with state of the art

As mentioned in Section 2, many detectors were introduced to detect the reflection symmetries of different kinds of objects. However, some of them [4, 2, 7, 8, 10, 39] have implementation codes that are available in the research community. For thorough discussions of reflection symmetry detection on binary shapes, we attempt to implement them on datasets (i.e., MPEG-7, UTLN-SRA, and UTLN-MRA), where their best settings along with the same thresholds (γ, μ) should be addressed for the shape analyses and evaluations. Hereunder, we comprehensively assess the performance of our shape-signature-based methods compared to those detectors'.

Table 5: Evaluation with the relevant metrics on MPEG-7.

Method	**Precision**	**Recall**	**F1-score**	$\mathbf{loss}_{\boldsymbol{\Delta}_\theta}$	$\mathbf{loss}_{\boldsymbol{\Delta}_d}$	***U-loss***	**Rank**
Loy *et al.* [7]	0.35417	0.25373	0.29565	0.41547	0.30501	0.53980	3
Cicconet *et al.* [4]	0.57377	0.51471	0.54264	0.55031	0.21706	0.62753	4
Gonzalez *et al.*[2]	0.47458	0.38356	0.42424	0.65869	0.43573	0.83881	5
Our $\mathcal{R}$-detector	0.89552	0.83333	**0.86331**	0.28151	0.17747	0.35500	2
Our LIP**-detector**	0.74324	0.77465	0.75862	0.22481	0.14526	**0.28494**	1

Note: The performance is ranked subject to *U-loss*.

5.5.1. Reflection symmetry detection on MPEG-7

It can be seen from Table 5 that our proposed detectors obtained the highest performance at both relevant metrics of F1-score and *U-loss*. Concretely, the $\mathcal{R}$-detector achieved 0.86331 and 0.355, respectively, better at least 32% than the others. In the meanwhile, the performances of the LIP-detector are a little less, with 0.75862 and 0.28494, respectively. They are about 10% lower than

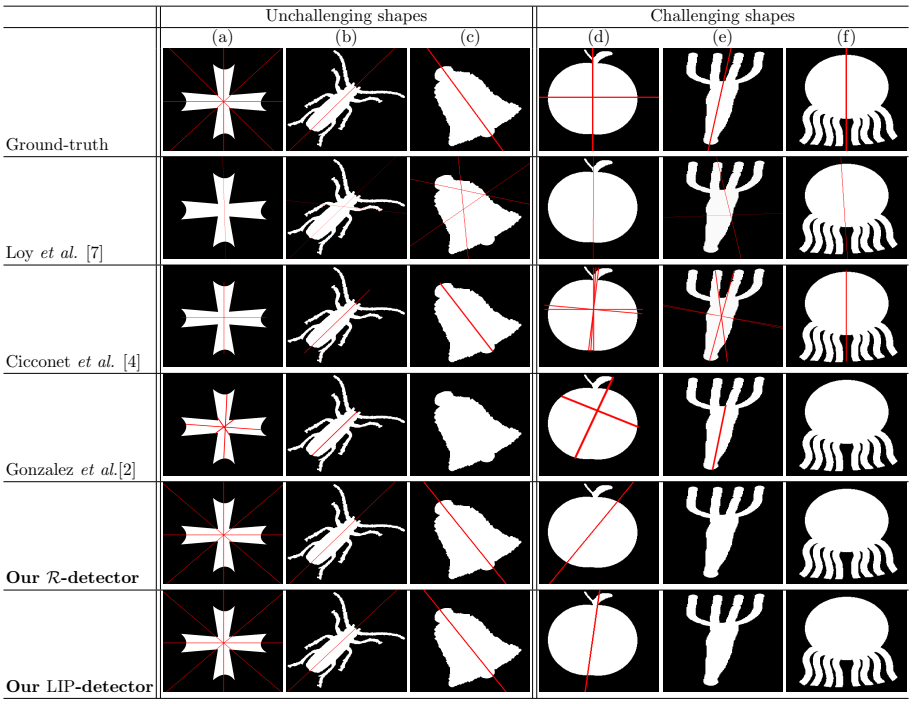

Figure 14: The unchallenging/challenging shapes of MPEG-7.

$\mathcal{R}$-detector's on F1-score but better on the measure *U-loss*. Fig. 14 shows some forms of the binary shapes which our detectors and the other methods did well in reflection symmetry detection as well as the shapes which have been challenging for future works to enhance the performance. Accordingly, it can be seen that the main reason leading to the unsuitable detections can be due to the indefinitely reflectional symmetry of the MPEG-7's shapes. For instance, both $\mathcal{R}$-detector and LIP-detector pointed out a misdirection axis on shape (d) in Fig. 14, while no axis was detected on shapes (e) and (f). It should be noted that the performances of Loy *et al.* [7] and Cicconet *et al.* [4] seem to be a little better than ours on three challenging shapes, but they are not on the unchallenging ones as well as on the others[5] of MPEG-7.

[5]For a visual view of all results of the methods on MPEG-7, it could refer to a supplementary material at `http://tpnguyen.univ-tln.fr/download/UTLN-Reflection/supplementary`.

Table 6: Evaluation with the relevant metrics on UTLN-SRA.

Method	Precision	Recall	F1-score	$\text{loss}_{\boldsymbol{\Delta}_\theta}$	$\text{loss}_{\boldsymbol{\Delta}_d}$	*U-loss*	Rank
Loy *et al.* [7]	0.975845	0.961905	0.968825	0.046360	0.023327	0.059159	6
Cicconet *et al.* [4]	0.995238	0.995238	0.995238	0.000635	0.007551	0.008015	3
Cicconet *et al.* [8]	0.928571	0.928571	0.928571	0.031720	0.009960	0.036914	5
Elawady *et al.* [10]	0.971429	0.971429	0.971429	0.031122	0.004036	0.032242	4
Cicconet *et al.* [39]	0.878049	0.857143	0.867470	0.083333	0.052865	0.106295	7
Our $\mathcal{R}$-detector	0.995240	0.995240	**0.995240**	0.000995	0.000003	**0.000998**	1
Our LIP**-detector**	0.995220	0.990480	0.992840	0.005743	0.004764	0.007718	2

Note: The performance is ranked subject to *U-loss*.

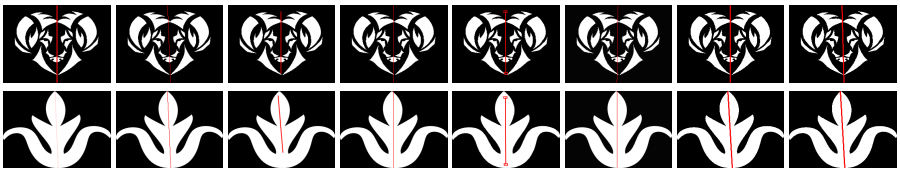

Figure 15: Results on the imperfect/absolute reflection symmetry shapes of UTLN-SRA. From the first column to the last one: Ground-truth; Loy *et al.* [7]; Cicconet *et al.* [4]; Cicconet *et al.* [8]; Elawady *et al.* [10]; Cicconet *et al.* [39]; **Our $\mathcal{R}$-detector; Our** LIP**-detector.**

5.5.2. Reflection symmetry detection on UTLN-SRA

It can be observed from Table 6 that all methods have significant detection results on the single-reflection shapes of UTLN-SRA. Specifically, with F1-score of 0.99524, our $\mathcal{R}$-detector is one of the best detectors, the same as the execution of Cicconet *et al.* [4]. It could be an absolutely alternative solution for the single-reflection symmetry detection. In the meanwhile, our LIP-detector obtained F1-score of 0.99284, only 0.25% lower than the $\mathcal{R}$-detector and Cicconet *et al.* [4]. Subject to the properties of *U-loss* measures, i.e. *U-loss* = 0.000998 for the $\mathcal{R}$-detector and *U-loss* = 0.007718 for the LIP-detector, ours are ranked at the highest levels of performance compared to the existing methods. In other words, our proposals are more suitable for reflection symmetry detection. Concretely, Fig. 15 indicates that our proposed detectors performed well in detecting reflection symmetry on two instances of compound shapes[6] (a) and (b) compared to the existing approaches. Indeed, for the imperfect symmetry shape Fig. 15(a), our proposal could point out the line which is more accurate

[6]For all detected results of the methods on UTLN-SRA, it could refer to the supplementary material at `http://tpnguyen.univ-tln.fr/download/UTLN-Reflection/supplementary`.

than the others [4, 8, 10, 7, 39], whose axis is slightly deviated to either the left or the right from the symmetry center line. The prominent performance is also for the absolute symmetry shape, as shown in Fig. 15(b). Those make our detectors have a small value of *U-loss*, i.e., ours could do better in general.

5.5.3. Reflection symmetry detection on UTLN-MRA

In terms of the symmetry detection on the multiple-reflection shapes of UTLN-MRA, our LIP-detector obtained the best performance in comparison with all existing methods[7]. Indeed, it can be seen from Table 7 that with F1-score of 0.93135 and *U-loss* of 0.14613, our LIP-detector is at least 18% better than the other approaches [7, 4, 8, 10, 39], and about 3% higher than the $\mathcal{R}$-detector. Fig. 16 shows that our LIP-detector executed well on all multiple-reflection shapes. In the meanwhile, most of the current approaches have been difficult to determine either which the right axes have been missing, such as the detection on shapes (a,b), or which the detected axes should be the absolutely reflectional symmetry. Indeed, for the detection on the unchallenging shapes (a,b,c), the notable detectors of Loy *et al.* [7], Cicconet *et al.* [8], Elawady *et al.* [10], and the $\mathcal{R}$-detector did well on shape (c) but two of them definitely failed on shapes (a,b). For the detection on the unchallenging shapes (d,e,f,g), only the detector of Cicconet *et al.* [8] and the $\mathcal{R}$-detector detected well on shape (f). Particularly, none of the state-of-the-art methods can point out all of the right axes of the gear shape (g). This may be due to the complicated attributes where the right reflection symmetries are located on both its teeth and non-teeth (see the ground-truth axes of the gear shape in Fig. 16(g)).

Consequently, it could be observed from Tables 6 and 7 that our LIP-detector should be recommended in practice for the detection issue of both single and multiple reflection symmetry shapes. That could be due to the better representation power of LIP-signature than $\mathcal{R}$-signature. In addition, since the F1-score measures of all methods on UTLN-MRA are at the modest levels (e.g., F1-score

[7]For all detected results of the methods on UTLN-MRA, it could refer to the supplementary material at `http://tpnguyen.univ-tln.fr/download/UTLN-Reflection/supplementary`.

Table 7: Evaluation with the relevant metrics on UTLN-MRA.

Method	Precision	Recall	F1-score	$\text{loss}_{\boldsymbol{\Delta}_\theta}$	$\text{loss}_{\boldsymbol{\Delta}_d}$	*U-loss*	Rank
Loy *et al.* [7]	0.81646	0.48224	0.60635	0.36875	0.34968	0.51387	5
Cicconet *et al.* [4]	0.78958	0.70315	0.74387	0.18767	0.12807	0.24650	3
Cicconet *et al.* [8]	0.28184	0.19403	0.22983	0.32355	0.37489	0.51929	6
Elawady *et al.* [10]	0.86612	0.58704	0.69978	0.34354	0.31045	0.48019	4
Cicconet *et al.* [39]	0.76905	0.53280	0.62949	0.80399	0.54154	1.02361	7
Our $\mathcal{R}$-detector	0.86528	0.93470	0.89865	0.14409	0.03899	0.16024	2
Our LIP**-detector**	0.92620	0.93657	**0.93135**	0.12973	0.03958	**0.14613**	1

Note: The performance is ranked subject to *U-loss*.

Table 8: Comparison of complexity and executing time on SRA.

Methods	Complexity	Time in average (s)
Loy *et al.* [7]	$O(N^4)$	0.36
Cicconet *et al.* [4]	$O(N^4 \log_2 N)$	15.62
Gonzalez *et al.* [2]	$O(N^2)$	-
Cicconet *et al.* [8]	$O(N^4)$	65.00
Elawady *et al.* [10]	$O(N^4)$	4.79
Cicconet *et al.* [39]	$O(N^4)$	110.56
Our $\mathcal{R}$-detector	$O(N^2 \log_2 N)$	3.87
Our LIP**-detector**	$O(N^2 \log_2 N)$	3.99

Note: The complexity is estimated in the worst case. "-" means not available.

of LIP-detector and $\mathcal{R}$-detector is 0.93135 and 0.89865 respectively), it could assure that the multiple-reflection shapes of UTLN-MRA have been challenging for the state-of-the-art detectors and perspectives. This restates the significant contributions of our proposed datasets for reflection symmetry detection.

5.6. Evaluation of computational complexity

Let us consider an input shape image of $N \times N$ pixels. Our proposed detectors are based on the construction of $\mathcal{R}$-signature and LIP-signature, which can be calculated in $O(|\Theta| \times N)$ time from its Radon image (refer to Alg. 2 for the processes in detail). Therein, $|\Theta|$ denotes the number of considered directions of projection ($|\Theta| = 180$ in practice). It is well-known that the Radon image can be calculated in $O(N^2 \log(N))$ using Fast Radon Transform [40]. The detection and verification of the candidates of symmetry direction are done in $O(|\Theta| + N)$, while the detection of the centroid is done in $O(N^2)$ by Alg. 1. Consequently, our proposed detectors have computational complexity of $O(N^2 \log(N))$.

For estimating the complexity of the previous works, because their detailed algorithms are not available, it is difficult to make an adequate complexity

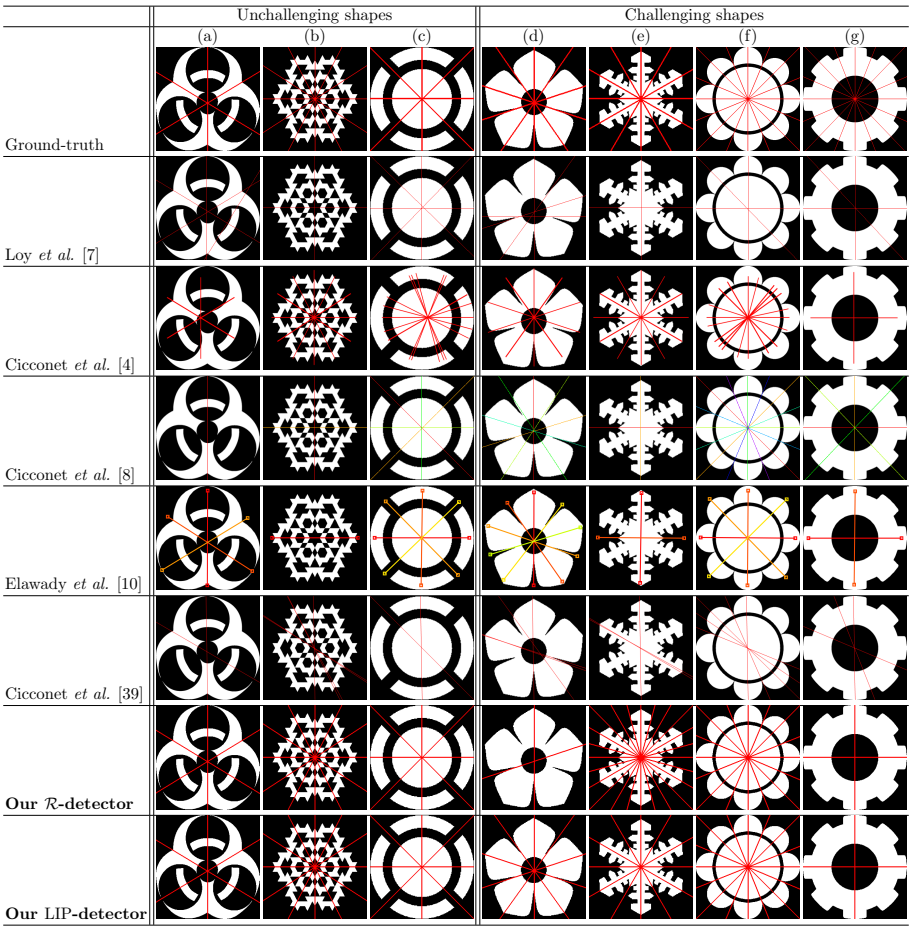

Figure 16: The unchallenging/challenging shapes of UTLN-MRA.

estimation. Therefore, we would like to conduct the complexity based on the primary detection steps in terms of the worst case (refer to the works [7, 4, 2, 8, 10, 39] for more detail of formulations and implementations). Table 8 presents the complexity of each method for detecting reflection symmetry on an $N \times N$ shape. Accordingly, the detector of Gonzalez *et al.* [2] requires the lowest resources with the complexity of $O(N^2)$, but it is not suitable for the analysis of the compound binary shapes, as thoroughly discussed in Section 5.4). In the meanwhile, the complexity of Cicconet *et al.* [4] has the highest cost with $O(N^4 \log_2 N)$. Ours is the second best level.

With respect to the processing time, we measure runtime of the detection process of our detectors compared to the competing methods[8]. Table 8 reports the mean execution time for the symmetry detection on a single-reflection shape of UTLN-SRA. Accordingly, with about 4s, our proposal is one of the lowest runtime levels. The detector of Loy *et al.* [7] is the speediest one (0.36s), but its detection performance is not good on the compound shapes, particularly the detection on the multi-axis ones, as thoroughly discussed in Sections 5.5.2 and 5.5.3. It should be noted that all implementations have been evaluated on a Windows 10 64-bit desktop computer with 3.5GHz CPU and 32GB RAM.

5.7. Analysis of reflection symmetry in natural images

Although the proposed approach is designed to mainly deal with shapes in binary images, we address hereafter several potential solutions to take into account reflection symmetry in natural images. Also, there are two main problems for this input data: single symmetry detection which determines the symmetry axis of the main symmetric object in an image, while multiple symmetry detection looks for the symmetric axis of multiple objects in the image. It should be noted that a good method on this input data should be tolerant against the deformation of an object or the negative impacts from the other objects in the natural images. Therefore, a preprocessing step of segmentation is necessary to make the detectors be more robust against those factors. Our main idea is to consider a deep-learning-based segmentation to extract the objects of interest and then to address our Alg. 2 to detect symmetric axes on every extracted object. Concretely, for the first problem, U2-Net [41] is used to segment the main object of the image thanks to its high performance in background removal, while an instant segmentation or a panoptic segmentation [42] is addressed for the second one. These solutions allow obtaining principle shapes in a real image for the symmetry detection. The last row of Figs. 17 and 18(a) shows the extracted results of U2-Net and panoptic segmentation on real images, respectively. Then,

[8]Except that Loy's detector [7] uses Python, other methods are developed using Matlab.

Algorithm 3 Reflection symmetry detection of a natural image I.

Input: I – a natural image, *mode* – TRUE: single, FALSE: multiple

if *mode* **then**
  $I_{seg} = I$ segmented by U2-Net.
else
  $I_{seg} = I$ segmented by Detectron2 for panoptic segmentation.
end if
for each $\mathcal{D} \in I_{seg}$ **do**
  Use Alg. 2 to detect symmetric axis of $\mathcal{D}$
end for

Figure 17: Symmetry detection on single ICCV'17 dataset. (a) and (b): results with LIP-signature and $\mathcal{R}$-signature, (c): shapes segmented by U2-Net from the corresponding images.

Alg. 3 is resumed on them for reflection symmetry detection. The first two rows of Figs. 17 and 18(a) show results of our detectors on several natural images in the single and multiple ICCV'17 dataset [1] by considering their corresponding segmented shapes resulted by the pre-trained models of U2-Net and the panoptic segmentation, respectively. It could be seen from this figure that our detectors give good results when the objects of interest are correctly segmented. In addition, Fig. 18(b) shows some complicated segmented shapes that our detectors have failed to locate the symmetric axes. Specifically, U2-Net does not give the satisfactory results if the scenes are almost background, while the papnoptic segmentation needs more similar scenes in the training phase to segment well the objects in the inference phase. Consequently, the above analyses along with the experiential results have proved the perspective of the proposed approach to deal with the reflection symmetry detection in natural images.

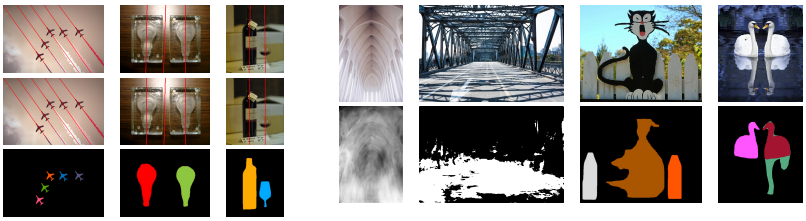

(a) (b)

Figure 18: (a): Symmetry detection on multi ICCV'17 dataset. The first and second rows are results of LIP-signature and $\mathcal{R}$-signature respectively, while the third row is input shapes segmented by panoptic segmentation. (b): Several complicated segmentation cases. The first row is input images; the last row shows the corresponding segmentation results where the first two columns are U2-Net's results and the rest are those of the panoptic segmentation.

6. Conclusions and perspectives

We have introduced two novel methods for reflection symmetry detection of shapes. Our proposals, which are robust against noise and deformation, can effectively deal with the compound shapes, which are challenging for the traditional contour-based methods. Also, two new datasets and a novel metric (*U-loss*) have been proposed for evaluating symmetry detectors. For future works, we will extend this framework to effectively deal with reflection symmetry in 3D shapes and in natural images, and also address the robustness of our proposal against affine, perspective, and non-rigid transformations.

Acknowledgments

We would like to thank Dr. Thai V. Hoang for the fruitful discussions. We express our gratitude to authors of the competing methods for sharing their codes. Also, we would like to send many thanks to those in Faculty of IT, HCMC University of Technology and Education, Ho Chi Minh City, Vietnam, who gave us crucial supports in high-performing computers for the experiments. Finally, we would like to thank the valuable remarks of the reviewers and editors.

Y.G. Kim and P.H. Truong were supported by the Institute of Information & communications Technology Planning & Evaluation (IITP), grant funded by the Korea government (MSIT) (No.2019-0-00231) as well as by the Basic Science

Research Program through the National Research Foundation of Korea (NRF) funded by the Ministry of Education (2020R1A6A1A03038540).

References

[1] C. Funk, S. Lee, M. R. Oswald, S. Tsogkas, W. Shen, A. Cohen, S. J. Dickinson, Y. Liu, ICCV challenge: Detecting symmetry in the wild, in: ICCVW, 2017, pp. 1692–1701.

[2] M. Alvarado-González, W. Aguilar, E. Garduño, C. Velarde, E. Bribiesca, V. Médina-Bañuelos, Mirror symmetry detection in curves represented by means of the slope chain code, Pattern Recognit. 87 (2019) 67–79.

[3] G. Marola, On the detection of the axes of symmetry of symmetric and almost symmetric planar images, IEEE Trans. Pattern Anal. Mach. Intell. 11 (1) (1989) 104–108.

[4] M. Cicconet, D. G. C. Hildebrand, H. Elliott, Finding mirror symmetry via registration and optimal symmetric pairwise assignment of curves, in: ICCVW, 2017, pp. 1749–1758.

[5] N. Widynski, A. Moevus, M. Mignotte, Local symmetry detection in natural images using a particle filtering approach, IEEE Trans. Image Process. 23 (12) (2014) 5309–5322.

[6] T. P. Nguyen, Projection based approach for reflection symmetry detection, in: ICIP, 2019, pp. 4235–4239.

[7] G. Loy, J. Eklundh, Detecting symmetry and symmetric constellations of features, in: ECCV, Vol. 3952 of LNCS, 2006, pp. 508–521.

[8] M. Cicconet, V. Birodkara, M. Lund, M. Werman, D. Geiger, A convolutional approach to reflection symmetry, Pattern Recognition Letters 95 (2017) 44 – 50.

[9] J. Bruna, S. Mallat, Invariant scattering convolution networks, IEEE Trans. PAMI 35 (8) (2013) 1872–1886.

[10] M. Elawady, C. Ducottet, O. Alata, C. Barat, P. Colantoni, Wavelet-based reflection symmetry detection via textural and color histograms, in: ICCV Workshops, 2017, pp. 1725–1733.

[11] D. J. Field, Relations between the statistics of natural images and the response properties of cortical cells, J. Opt. Soc. Am. A 4 (12) (1987) 2379–2394.

[12] A. Gnutti, F. Guerrini, R. Leonardi, Combining appearance and gradient information for image symmetry detection, IEEE Trans. Image Process. 30 (2021) 5708–5723.

[13] B. B. Chaudhuri, D. D. Majumder, Recognition and fuzzy description of sides and symmetries of figures by computer, Int. J. Syst. Sci. 11 (12) (1980) 1435–1445.

[14] S. K. Parui, D. D. Majumder, Symmetry analysis by computer, Pattern Recognition 16 (1) (1983) 63–67.

[15] H. Ogawa, Symmetry analysis of line drawings using the Hough transform, Pattern Recognition Letters 12 (1) (1991) 9–12.

[16] P. V. C. Hough, Method and means for recognizing complex patterns, U.S. Patent, no.3069654 (1962).

[17] R. K. K. Yip, A Hough transform technique for the detection of reflectional symmetry and skew-symmetry, Pattern Recognition Letters 21 (2) (2000) 117–130.

[18] Y. Lei, K. C. Wong, Detection and localisation of reflectional and rotational symmetry under weak perspective projection, Pattern Recognition 32 (2) (1999) 167–180.

[19] R. Nagar, S. Raman, Reflection symmetry axes detection using multiple model fitting, IEEE Signal Process. Lett. 24 (10) (2017) 1438–1442.

[20] R. Nagar, S. Raman, Detecting approximate reflection symmetry in a point set using optimization on manifold, IEEE Trans. on Signal Processing (2019).

[21] R. Nagar, S. Raman, Reflection symmetry detection by embedding symmetry in a graph, in: ICASSP, 2019, pp. 2147–2151.

[22] N. Kiryati, Y. Gofman, Detecting symmetry in grey level images: The global optimization approach, IJCV 29 (1) (1998) 29–45.

[23] H. Cornelius, M. Perdoch, J. Matas, G. Loy, Efficient symmetry detection using local affine frames, in: SCIA, Vol. 4522, 2007, pp. 152–161.

[24] S. Obdrzálek, J. Matas, Object recognition using local affine frames on distinguished regions, in: P. L. Rosin, A. D. Marshall (Eds.), BMVC, 2002, pp. 1–10.

[25] M. M. Kazhdan, B. Chazelle, D. P. Dobkin, A. Finkelstein, T. A. Funkhouser, A reflective symmetry descriptor, in: ECCV, 2002, pp. 642–656.

[26] S. Derrode, F. Ghorbel, Shape analysis and symmetry detection in gray-level objects using the analytical fourier-mellin representation, Signal Process. 84 (1) (2004) 25–39.

[27] F. Ghorbel, A complete invariant description for gray-level images by the harmonic analysis approach, Pattern Recognit. Lett. 15 (10) (1994) 1043–1051.

[28] P. E. Zwicke, I. Kiss, A new implementation of the mellin transform and its application to radar classification of ships, IEEE Trans. PAMI 5 (2) (1983) 191–199.

[29] E. Bribiesca, A geometric structure for two-dimensional shapes and three-dimensional surfaces, Pattern Recognition 25 (5) (1992) 483–496.

[30] E. Bribiesca, A measure of tortuosity based on chain coding, Pattern Recognition 46 (3) (2013) 716–724.

[31] S. R. Deans, The Radon Transform and Some of Its Applications, Krieger Publishing Company, 1993.

[32] M. Hasegawa, S. Tabbone, Amplitude-only log radon transform for geometric invariant shape descriptor, Pattern Recognition 47 (2) (2014) 643–658.

[33] T. P. Nguyen, T. V. Hoang, Projection-based polygonality measurement, IEEE Trans. Image Processing 24 (1) (2015) 305–315.

[34] T. P. Nguyen, X.-S. Nguyen, Shape measurement using LIP-signature, CVIU 171 (2018) 83–94.

[35] T. P. Nguyen, X. S. Nguyen, M. A. Borgi, M. K. Nguyen, A projection-based method for shape measurement, J. Math. Imaging Vis. 62 (4) (2020) 489–504.

[36] S. Tabbone, L. Wendling, J. Salmon, A new shape descriptor defined on the Radon transform, CVIU 102 (1) (2006) 42–51.

[37] S. M. Stigler, Francis Galton's Account of the Invention of Correlation, Statistical Science 4 (2) (1989) 73–79.

[38] L. J. Latecki, R. Lakamper, T. Eckhardt, Shape descriptors for non-rigid shapes with a single closed contour, in: CVPR, Vol. 1, 2000, pp. 424–429.

[39] M. Cicconet, D. Geiger, K. C. Gunsalus, M. Werman, Mirror symmetry histograms for capturing geometric properties in images, in: CVPR, 2014, pp. 2981–2986.

[40] W. A. Götz, H. J. Druckmüller, A fast digital Radon transform–An efficient means for evaluating the Hough transform, Pattern Recognition 28 (12) (1995) 1985–1992.

[41] X. Qin, Z. V. Zhang, C. Huang, M. Dehghan, O. R. Zaïane, M. Jägersand, U^2-net: Going deeper with nested u-structure for salient object detection, PR 106 (2020) 107404.

[42] Y. Wu, A. Kirillov, F. Massa, W.-Y. Lo, R. Girshick, Detectron2, `https://github.com/facebookresearch/detectron2` (2019).